Journal of Information and Computing Science
J. Info. Comput. Sci., Vol. 18, No. 2, pp. 81-100

DOI: 10.4208/JICS-2023-006
December 2023

Applications of Multifractal Detrended Fluctuation Analysis

Dongxu Dai[1,*], Yan Hu[1], Hao Qian[1], Guoqiang Qi[1], Renchang Sun[1], Jian Wang[1], Yan Wang[1], Hailong Lang and Minggang Li[1]

[1] *Benxi Power Supply Company of State Grid Liaoning Province Electric Power Co., Ltd., Benxi 117000, China*

Abstract. In recent years, multifractal detrended fluctuation analysis (MF-DFA) has become an important tool for detecting the scale and long correlation of non-stationary time series. With the continuous development of multifractal theory, researchers have widely applied it in physics, chemistry, biology, economy, etc. In this paper, we briefly review various applications of MF-DFA, and present some empirical research using one- and two-dimensional (2D) MF-DFA. 1D MF-DFA is always applied in financial markets, energy markets, heartbeat, and atmospheric science. Furthermore, 2D MF-DFA has been studied in surface science such as image segmentation, medical image classification. In this paper, we use 1D MF-DFA to explore the market efficiency of Korean stock market, and adopt 2D MF-DFA to segment images such as the license plate and hepatic cell image. In addition, we apply the proposed algorithm to segment transmission lines under icing condition, and the proposed method achieves satisfactory segmentation results.

AMS subject classifications: 28A80, 94A08

Key words: MF-DFA, Hurst exponent, Feature extraction, Image segmentation.

1 Introduction

Fractal phenomena are common in the natural and social sciences. Since Kantelhardt et al. [1] proposed the MF-DFA in 2002, this method has been successfully applied in various fields. The advantage of this method is that it can systematically filter out the trend components of each order, and can detect the correlation of the signal with noise.

*Corresponding author. *Email addresses:* ddxbben521@163.com (D. Dai), hy12768@163.com (Y. Hu), 1104891785@qq.com (H. Qian), qgq5697415637@163.com (G. Qi), src9694084531@163.com (R. Sun), wj3945216752@163.com (J. Wang), 745356941@qq.com (Y. Wang), 156745912@qq.com (H. Lang), 842675143@qq.com (M. Li)

In the past decades, one dimensional multifractal detrended fluctuation analysis (1D MF-DFA) has been widely used in financial markets such as stock markets [2], exchange markets [3], crude oil markets [4], and Bitcoin market [5]. Matia et al. [6] used this method to study the daily closing prices of 2449 stocks and 29 commodities for the past 15 years. As a result, it was found that both stock prices and commodity prices have multifractal characteristics, and that the multifractal spectrum of stock prices is significantly narrower than the multifractal spectrum of commodity prices, indicating that commodity price fluctuations have a strong correlation. Drożdż [7] forecasted the two world-leading stock market indices such as the S&P500 and NASDAQ based on the long-term records and results showed that multifractal features existed. However, the characteristics evolve through shapes, most of them are strongly asymmetric. Shao and Wang [8] applied the MF-DFA to study the difference in financial market of South Korea before and after South and North Korean leaders' meeting on April 27, 2018. The results showed that multifractality existed in all time intervals for both the markets, and the multifractal characteristics after the meeting were stronger, which indicated that before the meeting, the financial markets have a higher market efficiency, and decreased after the meeting. They concluded that the meeting of South and North Korean leaders since April 27, 2018 was a possible interpretation for changes of efficiency in South Korean financial markets. Moreover, Lahmiri and Bekiros [9] investigated the multifractal chaotic dynamics of Islamic and Green crypto-currency series in econophysics literature. Their findings indicated that the price, volatility and volume series of Islamic and green crypto-currencies embed high persistence compared to the conventional crypto-currencies. Chen [10] analyzed the time series of the WTI and Brent Crude oil spot prices series from 1987 to 2008. The analysis results indicated that range Hurst exponent and Renyi exponent were changed by the steps change of time series, and there were multifractal characteristics in international crude oil spot price systems. Recently, many studies on air pollutants have been conducted and the results have suggested that the increased levels of $PM_{2.5}$ are associated with a higher mortality and some negative effects on the lungs [11]. Wang et al. [12] investigated the implications of "Haze Special Law" on air quality in South Korea. The authors found that the multifractality after the implementation of the law was weaker than that before the law for all the cities, which shows that the enactment of the law has played a role in improving the efficiency of air pollution control in South Korea. There were also some multifractal research related to meteorological factors studied in [13, 14].

Moreover, 1D MF-DFA has been widely applied in the field of heart rate dynamics in the past decades. By analyzing the multifractal spectrum of human heart rate, many important conclusions have been used in clinical diagnosis. Ivanov et al. [15] found the multifractal properties and nonlinear characteristics of the heart rate of healthy human heartbeat and encode it in the Fourier phases. In addition to adults, MF-DFA is also used to provide elaborated and detailed analysis of FHR [16].

In addition, many achievements have been made in the application of fractal theory in image field. Especially, for image segmentation field, past works [17–20] have shown multiple ways to make this method feasible. Research shows that it is not enough to describe complex non-linear systems by only one fractal dimension. Local conditions are very important in the formation of complex structures. In order to further understand the role of local conditions in the formation of fractal bodies, a multifractal method is proposed in [21]. Based on multifractal spectrum,

Jin [22] performed the algorithm based on capacity measurement and probability measure for image segmentation. Yu [23] applied multifractal theory combined with fractal Brownian motion in CT image edge detection. As a meaningful extension of 1D MF-DFA, Gu [24] used the 2D MF-DFA to analyze multifractal surfaces. Since then, 2D MF-DFA has been used for some studies to implement for some specific image analysis [25–27]. For instance, Wang et al. [28] segmented leaf image segmentation method based on 2D MF-DFA. They demonstrated the proposed method was more effective and provide more robust segmentation on recognizing the lesion regions, when compared with other two segmentation methods. Furthermore, the 2D multifractal techniques are also effective for handling magnetic resonance image segmentation [29]. The local Hurst exponent obtained by using 2D MF-DFA can also be used as image features. In our study of the classification for retinal fundus images [30], the lesion area of the retinal fundus image can also be accurately segmented, as shown in Figure 1. Figure 1(a) is selected from the diabetic retinopathy database, please refer to "http://www.it.lut.fi/project/imageret/diaretdb0".

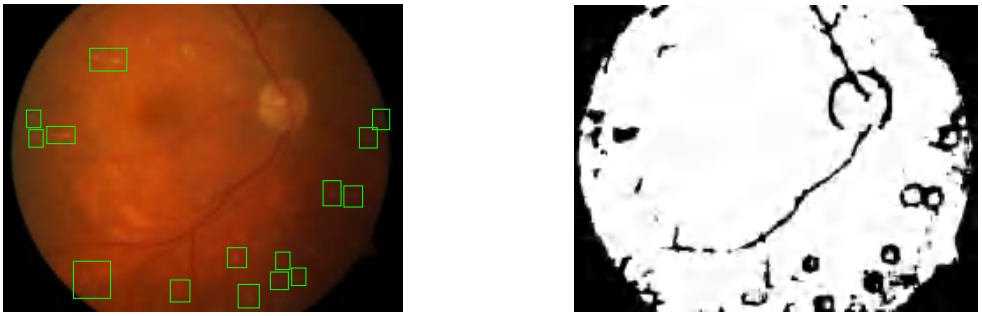

(a) (b)

Figure 1: Lesion regions segmentation of retinal fundus image.

This paper is organized as follows. In Section 2, we introduce 1D MF-DFA method. The empirical example of 1D MF-DFA is studied in Section 3. In Section 4, we describe the methodology of 2D MF-DFA. In Section 5, we present various empirical research of 2D MF-DFA. Finally, conclusions are provided in Section 6.

2 Methodology of 1D MF-DFA

Let x_k $(k=1,2,\ldots,N)$ be a series. The algorithm of 1D MF-DFA can be divided into five steps.
Step 1: Construct a summation sequence

$$Y(i)=\sum_{k=1}^{i}(x_k-\bar{x}),\quad i=1,2,...,N, \tag{2.1}$$

where $\bar{x}=\sum_{k=1}^{N}x_k/N$ is the mean of x_k. For example, let X_k $(k=0,1,2,\ldots,365)$ be a time series of closing stock prices for each business day from August 31, 2018 to February 28, 2020, see Figure

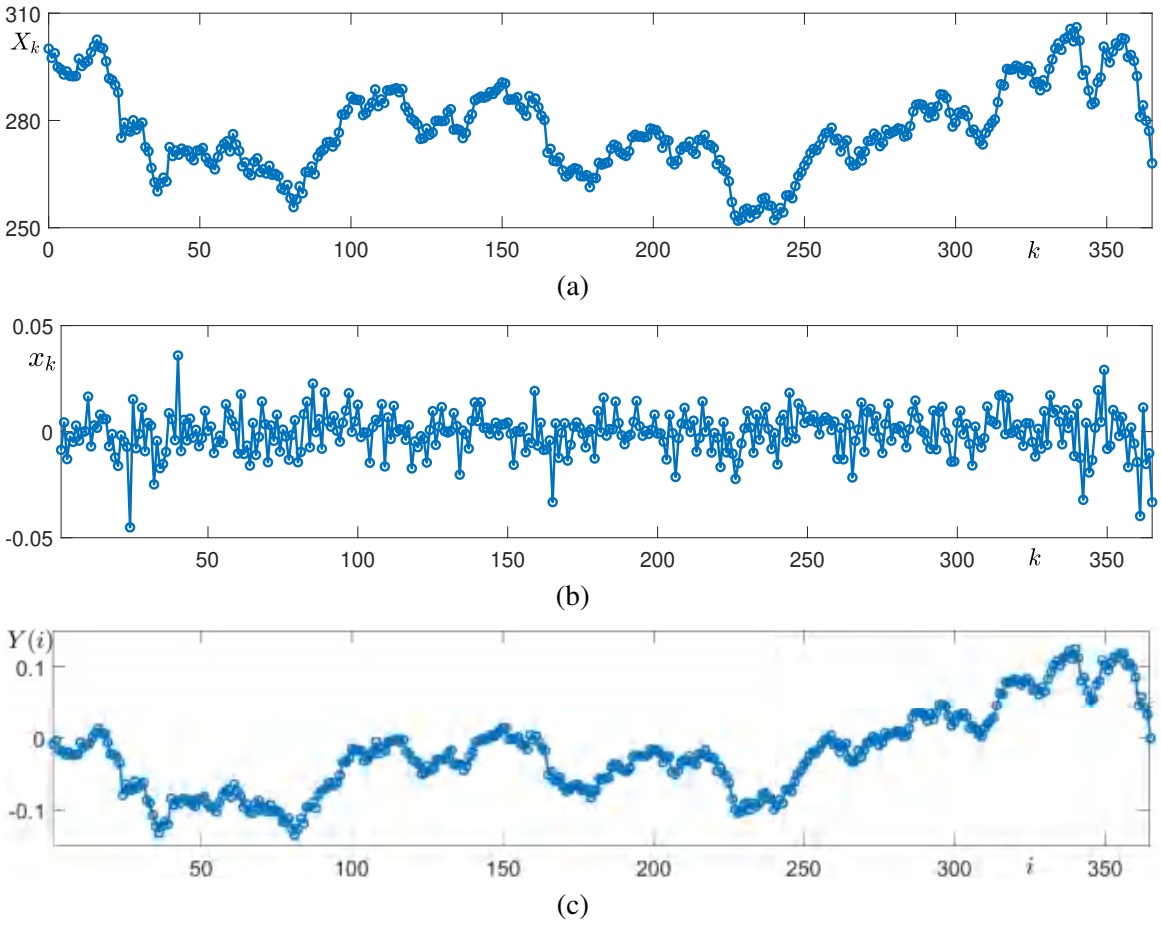

Figure 2: Time series of (a) closing stock prices X_k, (b) logarithmic return x_k, and (c) $Y(i)$.

2(a). We define the logarithmic return $x_k = \ln X_{k+1} - \ln X_k$, $(k = 1,2,\ldots,365)$ and illustrate it in Figure 2(b). Then, $Y(i)$ is shown in Figure 2(c).

Step 2: Starting from index $i = 1$, divide $Y(i)$ into $N_s = [N/s]$ disjoint intervals of length s, where $[x]$ is the largest integer that is less than or equal to x. Next, starting from index $i = N$, divide $Y(i)$ into N_s disjoint intervals of length s. From this procedure, we obtain $2N_s$ segments. For example, let $s = 10$, then $N_s = 36$ and we have $2N_s = 72$ segments as follows.

$$\{Y(1),\ldots,Y(10)\},\ \{Y(11),\ldots,Y(20)\},\ \cdots,\{Y(351),\ldots,Y(360)\}, \tag{2.2}$$

$$\{Y(356),\ldots,Y(365)\},\ \{Y(346),\ldots,Y(355)\},\ \cdots,\{Y(6),\ldots,Y(15)\}. \tag{2.3}$$

Step 3: Define the variance

$$F^2(v,s) = \frac{1}{s}\sum_{i=1}^{s}[Y((v-1)s+i)-y_v(i)]^2, \text{ for each segment } v=1,\ldots,N_s, \tag{2.4}$$

$$F^2(v,s) = \frac{1}{s}\sum_{i=1}^{s}[Y(N-(v-N_s)s+i)-y_v(i)]^2, \text{ for each segment } v=N_s+1,\ldots,2N_s, \tag{2.5}$$

where $y_v(i)$ is a least-squares fitting polynomial in segment v. That is,

$$y_v(i) = a_m i^m + a_{m-1} i^{m-1} + \cdots + a_1 i + a_0, \tag{2.6}$$

where $i = 1, 2, \ldots, s$, $v = 1, 2, \ldots, 2N_s$, and $m = 1, 2, \ldots$. For example, we take $s = 10$ and choose the third segment among $2N_s$. Then, calculate Y, y_v, $Y - y_v$ and $F^2(v,10)$ and illustrate them as shown in Figure 3. Here, we use $m = 1, 2, 3$.

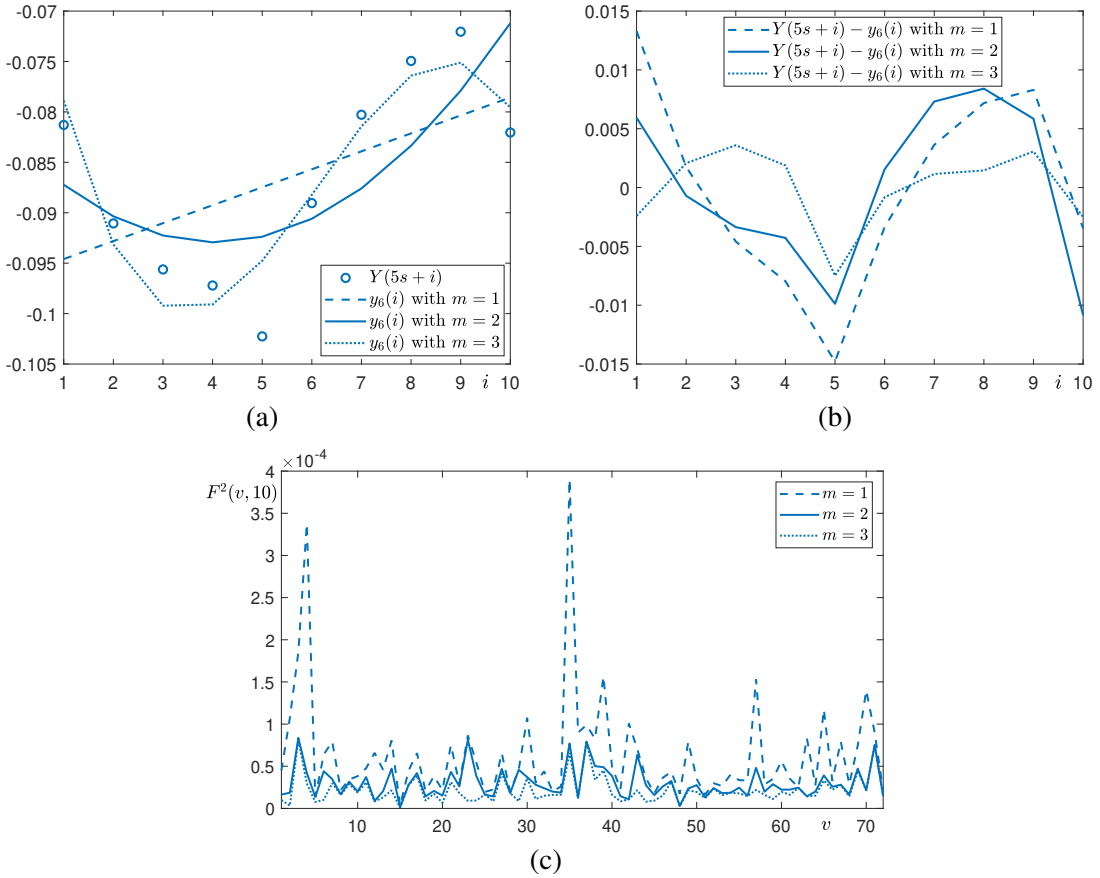

Figure 3: Plots of (a) Y and y_v, (b) $Y - y_v$, and (c) $F^2(v,10)$ with $m = 1, 2, 3$.

Step 4: Compute the qth order fluctuation function

$$F_q(s)=\begin{cases}\left\{\frac{1}{2N_s}\sum_{v=1}^{2N_s}[F^2(v,s)]^{q/2}\right\}^{\frac{1}{q}} & \text{if } q\neq 0,\\ \exp\left\{\frac{1}{4N_s}\sum_{v=1}^{2N_s}\ln[F^2(s,v)]\right\} & \text{if } q=0.\end{cases} \tag{2.7}$$

Figure 4 shows $F_q(s)$ when we use $m=2$, $q=-10,\ -5,\ 0,\ 5,10$, responding from the bottom curve to the top curve, $s=5,6,\ldots,14,15$.

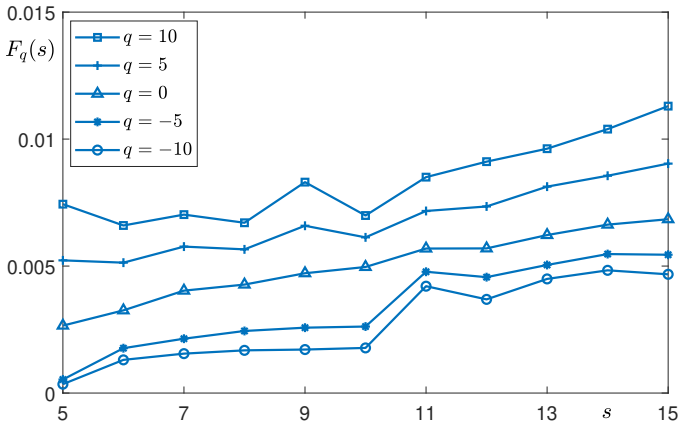

Figure 4: Plot of $F_q(s)$

Step 5: Determine the scaling behavior of $F_q(s)$ by analyzing log-log plots $F_q(s)$ versus s for each value of q.

If the series x_i is long-range power-law correlated, then $F_q(s)$ satisfy the following power-law relation for large values of s:

$$F_q(s)\sim s^{H(q)}, \tag{2.8}$$

which implies $F_q(s)=Cs^{H(q)}$ for some constant C and taking logarithms of both sides results in

$$\ln F_q(s)=H(q)\ln s+\ln C. \tag{2.9}$$

The Renyi exponent $\tau(q)$, which is related to the general Hurst exponent can be expressed by

$$\tau(q)=qH(q)-1, \tag{2.10}$$

in addition,

$$\alpha=H(q)+qH'(q), \tag{2.11}$$

$$f(\alpha)=q[\alpha-H(q)]+1, \tag{2.12}$$

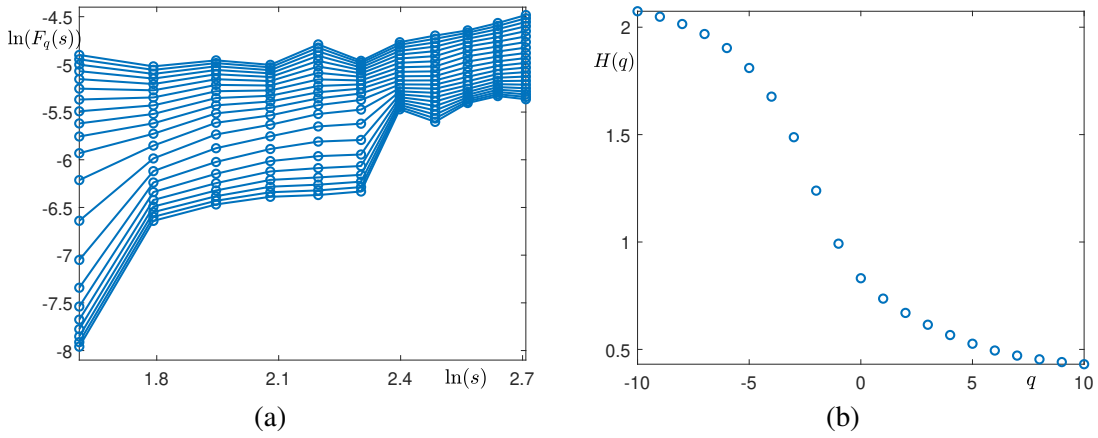

Figure 5: (a) Log-log plot of $F_q(s)$ versus s for each value of q. (b) Plot of $H(q)$ versus q.

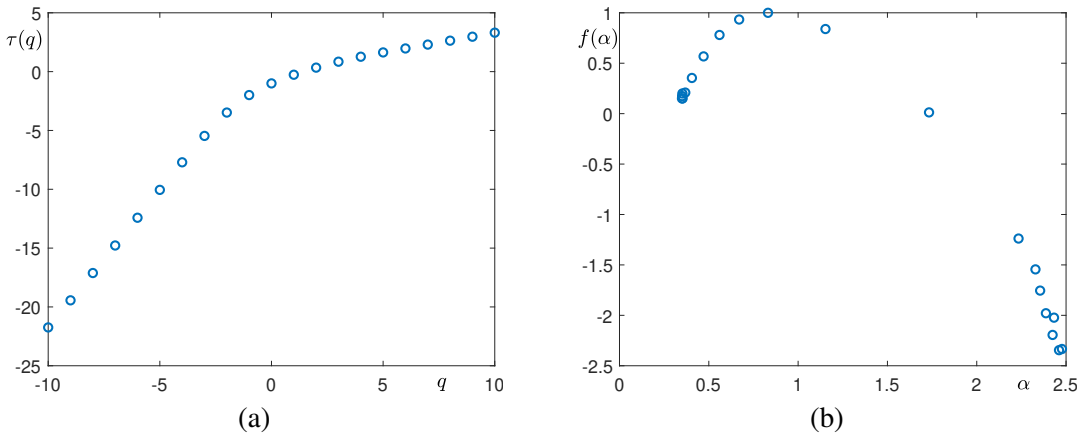

Figure 6: Plots of (a) $\tau_q(s)$ versus q and (b) $\alpha(q)$ versus α.

where α represents the Holder exponent and characterizes the singularity strength, and $f(\alpha)$ is a fractal dimension of the set of points with particular α. In the plotted curve between α and $f(\alpha)$, the shape resembles an inverted parabola, and the degree of their complexity is denoted by the width of their fractal strength $\Delta\alpha$ [31].

Through the analysis of double log plots of $F_q(s)$ versus s and a varied q, the scaling behavior of the fluctuation is determined by the power-law $F_q(s) \propto s^{H(q)}$, and from this, a family of scaling exponents $H(q)$, which are generalized Hurst components, can be obtained. $F_q(s)$ is the standard DFA, if $q = 2$. The Hurst exponents provide information on the time series, such as power-law correlated behavior, and when $0 < H(q) < 0.5$, it indicates that the time series has a negative or anti-persistence property. When $0.5 < H(q) < 1$, then the time series has a positive persistence, and $H(2) = 0.5$ indicates the time series has an uncorrelated Brownian process.

3 Empirical research of 1D MF-DFA

In our study, we choose the daily closing price of KOSPI200 for multifractal analysis. The data of KOSPI200 price is collected from 26 May 2010 to 26 May 2020, which consists of 2467 data points, after excluding non-trading days (weekends and holidays). The data are obtained from "https://kr.investing.com/indices/kospi-historical-data". The time series of KOSPI200 is shown in Figure 7.

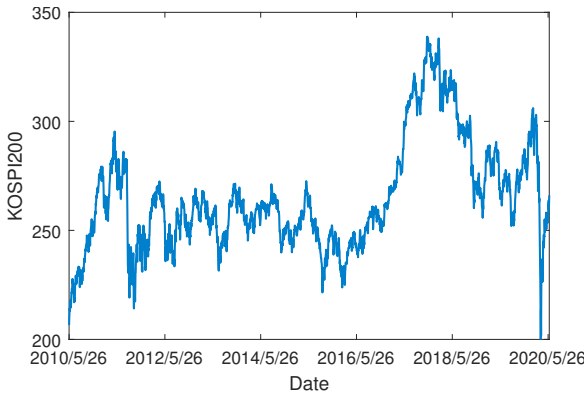

Figure 7: Time series of KOSPI200.

We then calculate the daily returns which can be denoted by differentiating the log value of the KOSPI200 time series, and the daily returns are shown in Figure 8. By the first step of MF-DFA, we first construct a cumulative dispersion series from 1 to 2466, which is shown in Figure 9.

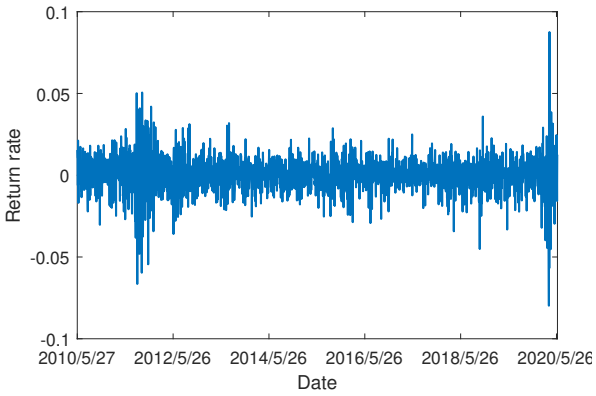

Figure 8: Log differences time series of KOSPI200.

According to [32], we choose parameters such as q varied from -10 to 10 with an increment of 1, and scale size s is selected from 5 to 35 with a increment of 3. According to the calculation process in Section 2, we depict the log-log plots of the fluctuation function $F_q(s)$ versus the time scale s of the return series of KOSPI200 in Figure 10(a). We note that $F_q(s)$ increases linearly

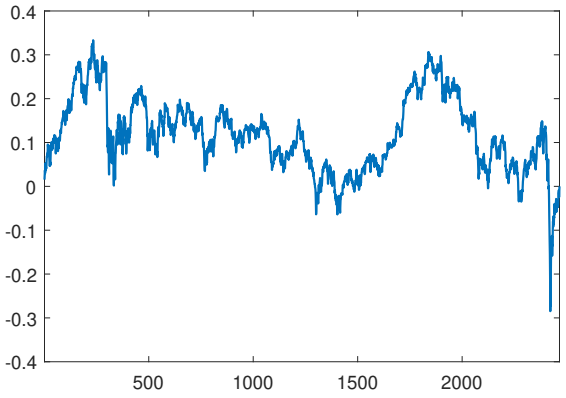

Figure 9: Cumulative dispersion series of return series.

as the scale s size increases, which shows that there exists power law behavior and multifractal features for the return series of KOSPI200. From Figure 10(b), we observe that when the Hurst exponent $H(q)$ varies with different values of q, thus, the return series of KOSPI200 is multifractal, otherwise, it is monofractal.

Besides, we also find that with q varying from -10 to 0, $H(q)$ decreased rapidly, while q varying from 0 to 10, $H(q)$ decreased slowly, implying the price behavior of small and large fluctuations. Specifically, the Hurst exponent $H(2) > 0.5$, indicating that there are strong positive persistent behaviors for return series of KOSPI200. The multifractal degree of the time series can be described by $\Delta H = H_{max} - H_{min} = 1.1066$. Furthermore, the Renyi exponent $\tau(q)$ versus q is estimated in Figure 10(c). The curve is non-linearly dependent on q, which provides further evidence of multifractality. Finally, we calculate α and the multifractal spectrum $f(\alpha)$ in Figure 10(d). If a multifractal spectrum appears as a point, it is monofractal; otherwise, it is multifractal. Figure 10(d) reveals that multifractality exists in return series of KOSPI200. The multifractal extent of the time series can also be represented by the width of α, which is calculated by $\alpha_{max} - \alpha_{min} = 1.4436$.

In addition, we calculate $\Delta f = f(\alpha_{min}) - f(\alpha_{max})$. If $\Delta f > 0$, the curve is left hook, then it indicates that the probability of return rate of KOSPI200 price at the highest price is greater than that at the lowest price. In our results, we see that $\Delta f > 0$, which means that, at present, the return rate of KOSPI200 price is at a high level.

4 Methodology of 2D MF-DFA

As an extension of the 1D MF-DFA method, the 2D MF-DFA method expands the 1D MF-DFA analysis of time series to the analysis of 2D image. Figure 1(a) is taken as an example for introduction in this section. The procedure of 2D MF-DFA can be conducted as follows.

I. Set the image in the size of $A \times B$, and the Figure 1(a) is transferred to a 2D gray image with size $A \times B = 130 \times 100$ shown in Figure 11.

As the generalized Hurst exponent described in Section 2, for 2D MF-DFA, the $h(q)$ can

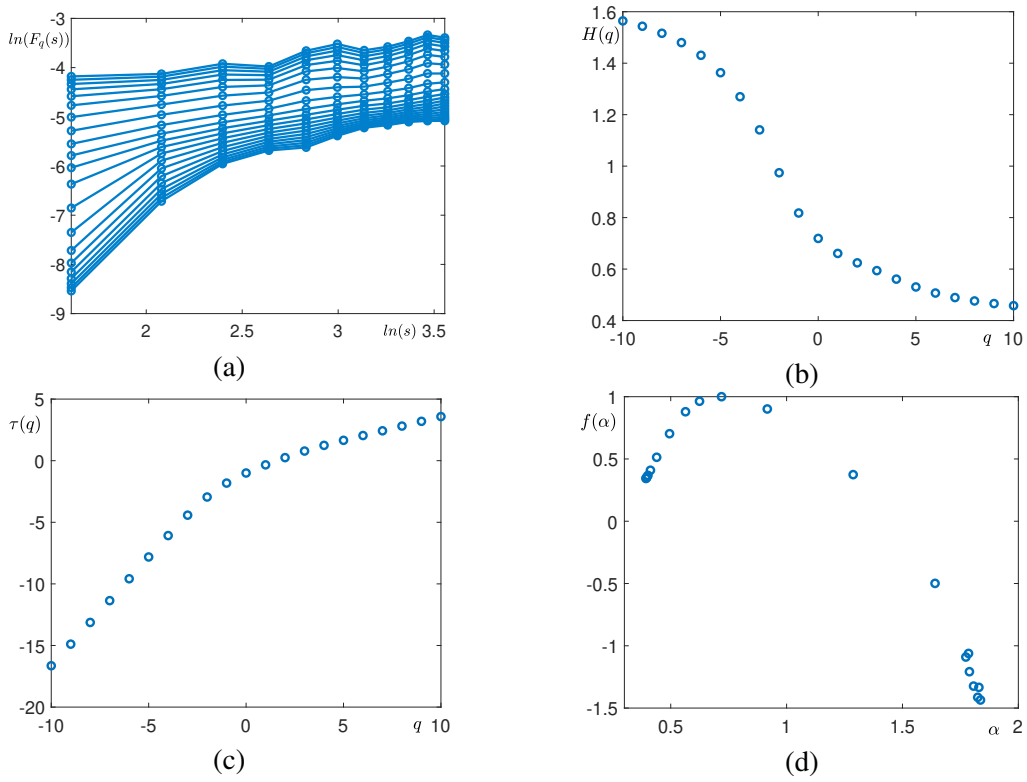

Figure 10: (a) Log-log plots of $F_q(s)$ versus s, (b) Hurst exponent, (c) Renyi exponent, and (d) multifractal spectra for return series of KOSPI200.

represent the image natures, which is called the local $h(q)$, expressed as $L_{h(q)}$. We can segment different regions by changing the value of $L_{h(q)}$. On each pixel (i,j), we use a $v\times v$ moving window centered at (i,j) to calculate $L_h(q)$ in that window, and consider it as the feature of the pixel centered at (i,j). The $L_{h(q)}$ of each pixel can be obtained with the window slides from left to right and top to bottom on each pixel. In this study, we use the window size $v\times v=11\times 11$, as shown in Figure 12.

After sliding from left to right and top to bottom centered at each pixel, a total number $A-v+1\times B-v+1$ of $L_{h(q)}$ can be obtained. As shown in Figure 13, each point centered at pixel represents a $L_{h(q)}$.

II. Considering every sliding window as a sub-image with size $I\times J=v\times v$, and discretizing it into matrix $x_{i,j}$, $i=1,2,\ldots,I$, and $j=1,2,\ldots,J$.

As same as the 1D MF-DFA, the sub-image is divided into non-overlapping sub-regions with a varied length s, then a size of $I_s\times J_s$ can be obtained, I_s and J_s are the largest integers less than I/s and J/s, respectively. Define each sub-region as $x_{m,n}(i,j)=x((m-1)s+i,(n-1)s+j)$, where i

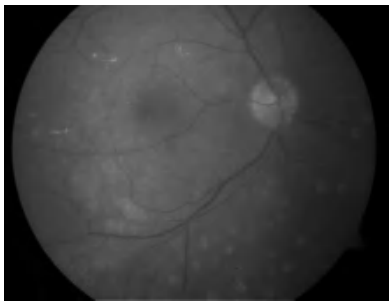

Figure 11: Gray image of the original retinal fundus image.

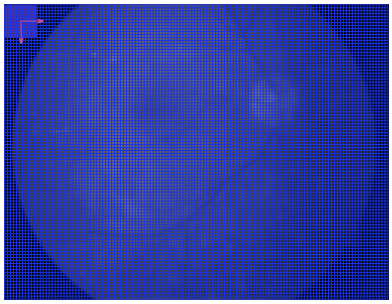

Figure 12: Initial state of sliding window with size of 11×11 in the retinal fundus image.

and j satisfy $1\leq i,\ j\leq s$, then

$$U_{m,n}(i,j)=\sum_{k_1=1}^{i}\sum_{k_2=1}^{j}x_{m,n}(k_1,k_2), \tag{4.1}$$

where $U_{m,n}(i,j)$ is the cumulative sum of surface pixels in each sub-region. For example, we take s from 2 to 4, then each sub-image can be divided into $I_s\times J_s=5\times5$, 3×3, and 2×2 sub-regions, respectively to $s=2$, 3, and 4, as shown in Figure 14.

III. Using the least-squares method to fit the k-th polynomial $U_{m,n}(i,j)$ in each sub-region. Here, the plane $\bar{U}_{m,n}(i,j)$ is adopted, and $\bar{U}_{m,n}(i,j)=ai+bj+c$ is taken with polynomial order $k=1$. Then $u_{m,n}(i,j)$ in residual matrix is defined as

$$u_{m,n}(i,j)=U_{m,n}(i,j)-\bar{U}_{m,n}(i,j). \tag{4.2}$$

IV. Obtaining the detrended fluctuation function $F^2(m,n,s)$ in each sub-region, where

$$F^2(m,n,s)=\frac{1}{s^2}\sum_{i=1}^{s}\sum_{j=1}^{s}(u_{m,n}(i,j))^2. \tag{4.3}$$

Then the fluctuation function in each sub-region is

$$F_q(s)=\left\{\frac{1}{I_sJ_s}\sum_{m=1}^{I_s}\sum_{n=1}^{J_s}[F(m,n,s)]^q\right\}^{\frac{1}{q}}. \tag{4.4}$$

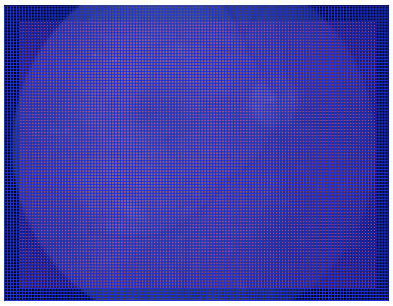

Figure 13: Routes passing points of sliding window in the retinal fundus image.

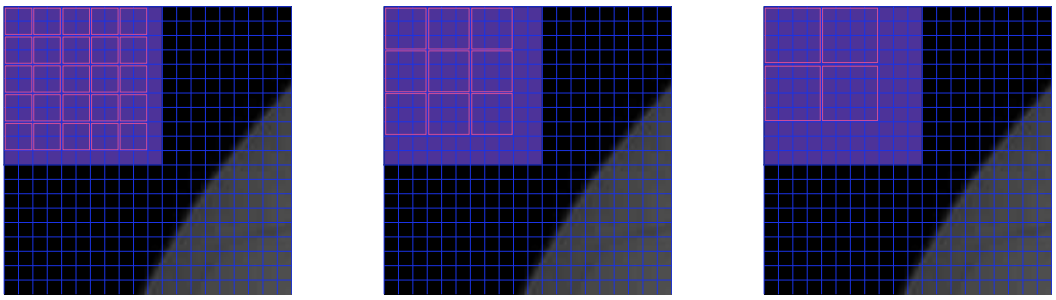

(a) (b) (c)

Figure 14: Sub-regions conditions of sub-image when (a) $s=2$, (b) $s=3$, and (c) $s=4$.

When $q=0$,

$$F_q(s)=\exp\left(\frac{1}{I_sJ_s}\sum_{m=1}^{I_s}\sum_{n=1}^{J_s}\ln[F(m,n,s)]\right). \tag{4.5}$$

V. Finally, the scaling behavior of the fluctuation is determined by a varied range s, and a set of power relations between $F_q(s)$ and scales s can be obtained by

$$F_q(s)\propto s^{h(q)}. \tag{4.6}$$

Here, q is fixed as 10. The log-log plots of fluctuation function $F_q(s)$ versus s and the straight line fitted by least squares method are depicted in Figure 15.

Repeat this process by sliding the window from left to right and top to bottom for the original retinal fundus image, then we can obtain $L_{h(q)}$ with a total number of 120×90, we plot the values of $L_{h(q)}$ with sliding window centered at different locations in Figure 16.

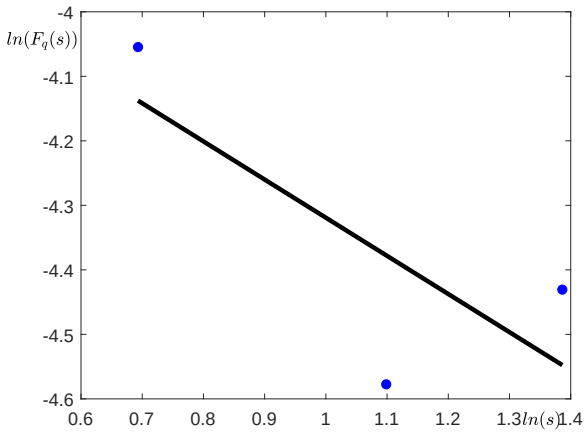

Figure 15: Log-log plots of the first sub-image.

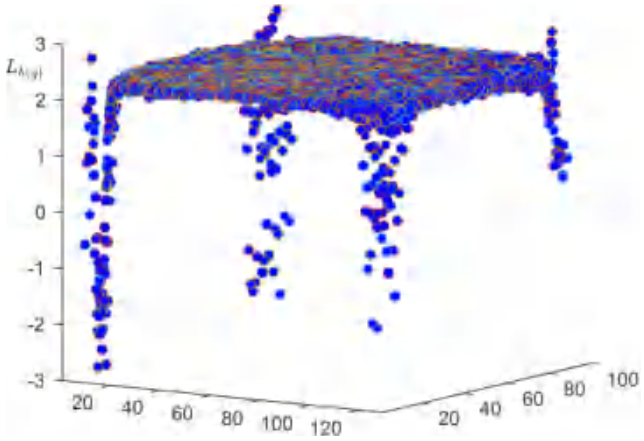

Figure 16: Values of $L_{h(q)}$ with sliding window centered at different locations.

For segmenting the image, we construct an interval $[L_{h(q_{min})}, L_{h(q_{max})}]$ with the maximum and minimum values of the $L_{h(q)}$. Then divide the interval into n equal segments and use the box counting method to calculate the fractal dimension of a sub-image composed of specific $L_{h(q)}$. By such steps, we can obtain a series of fractal dimensions $d_1(L_{h(q)})$, $d_2(L_{h(q)})$, $\ldots$, $d_n(L_{h(q)})$ and $n = 30$ is selected in this study.

We cover a region in the sub-image by using the box size $\alpha \times \alpha$. If $L_{h(q)}$ belongs to the considered interval, we record the number. The total number of boxes $N(\alpha)$ will be recorded as the box slides over all the sub-image. Finally, a series of $N(\alpha)$ can be calculated by the power law

$$N(\alpha) = \left(\frac{1}{\alpha}\right)^{-d}, \tag{4.7}$$

with the change of the size of $\alpha\times\alpha$. The spectrum $d(L_{h(q)})$ of 2D MF-DFA is obtained as

$$d(L_{h(q)})=\lim\frac{\ln N(\alpha)}{\ln(1/\alpha)}. \tag{4.8}$$

In this paper, α is chosen by 2,4,8,16, and 32. The singularity of the image can be determined according to the value of $d(L_{h(q)})$. As the $d(L_{h(q)})$ value closer to 1, the smoother boundary points corresponding to pixels. With the value closes to 2, the corresponding pixels located on the smooth surface. In addition, the Renyi exponent, Holder exponent, and the fractal dimension of 2D MF-DFA are calculated as same as 1D MF-DFA.

5 Empirical research of 2D MF-DFA

In this section, we perform various experiments to show the robustness and efficiency of 2D MF-DFA. In the first test, we generate a simple synthetic grid image which consists of grids with different colors as shown in Figure 17(a). As the first step of edge segmentation, we transfer the original image to a two-dimensional gray image. The gray image and the ideal or reference segmented image of Figure 17(a) are the one in Figure 17(b) and the one in Figure 17(c), respectively. The result of an edge image based on the MF-DFA is shown in Figure 17(d). The pixel of Figure 17(a) is taken by 410×550, the parameters in this test are set as $v\times v=11\times11$ and the segment scales are 2,3,4, and 5. The edge segmentation is based on the local Hurst index by $L_{h(q)}=L_{h(10)}$.

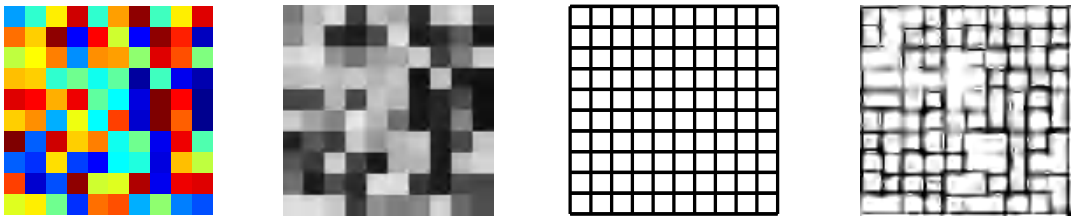

(a) (b) (c) (d)

Figure 17: (a) Original target image, (b) gray image of original image, (c) reference segmented image, and (d) result of proposed method.

License plate recognition plays an essential role in daily life, which is embodied in automatic toll collection, traffic law enforcement, parking solutions and so on. Next, we perform the edge detection experiment using 2D multifractal technique on license plates. For this case study, we present three different cases for license plates which are involved in illumination variation cases of two different extent and Gaussian noise ($\mu=0$, $\sigma=0.2$). The pixel for each license plate image is 526×178, the window size is selected by 11×11 and the segment scales are the same to the above test. Here, the order q in $L_{h(q)}$ is used by $q=10$.

By using 2D MF-DFA to test license plate recognition, we have achieved satisfactory results, as well as the case of illumination changes. When Gaussian noise is added to the original image, the method also shows a good performance for processing unstable image, this implies that our method has strong anti-noise ability, which are shown in Figure 18.

Figure 18: (a) Original images with bright, dusky, and Gaussian noise from left to right, respectively, (b) three corresponding segmentation results.

Segmentation of medical images from CT, MRI, and cell structure under microscope plays a particularly important role in the treatment strategies for clinical diseases. In the last segmentation case, we apply the proposed model to the segmentation of hepatic cells. In addition, in order to check the accessibility of the results obtained by MF-DFA method, we study the difference of multifractal characteristics between the normal hepatic cell and the hepatic cell of fatty liver as shown in Figure 19. Figure 19(a) refers to the normal hepatic cell and Figure 19(b) refers to the hepatic cell of fatty liver. The pixel sizes of both the two images are 225×225. For the segmentation process, we set parameters as $v\times v=7\times7$, $q=10$, and segment scales $s=2$ and 3. The interval of spectrum is taken by $[1.41,1.95]$.

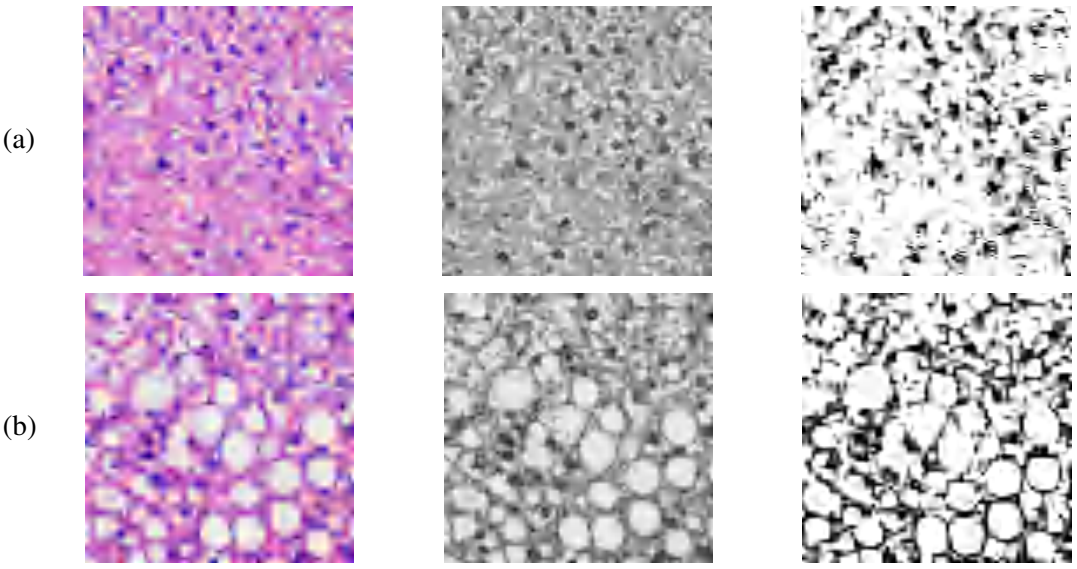

Figure 19: Edge extraction process for hepatic cells, (a) normal hepatic cell, (b) hepatic cell of fatty liver. The original images in the first column are obtained from C. Maillo et al. [33].

Next, we analyze multifractal features and spectrum of the above two hepatic cells. There are fat vacuoles in the liver cell images, which lead to sharp changes in the local gray level and unstable gray distribution. Therefore, it is necessary to study the multifractal characteristics of the two images. When calculating the multifractal spectrum, the parameters are segment scale s and fractal order q. We set the minimum segment scale $s_{min}=2$, the maximum segment scale

$s_{max}=(M-1)/2$. For this case, the segment size in total is 111. The fractal order q is taken from -10 to 10.

To find whether there exists a linear relationship between the double-log plots of s and $F(q,s)$ is the first step of multifractal analysis. As shown in Figure 20, the log-log plots of fluctuation function versus q are plotted from $q=-10$ to $q=10$. The decreasing slope with the increasing of q indicates that both the two images have multifractal characteristics. Figure 19(a) and (b) refer to the normal hepatic cell and hepatic cell of fatty liver, respectively.

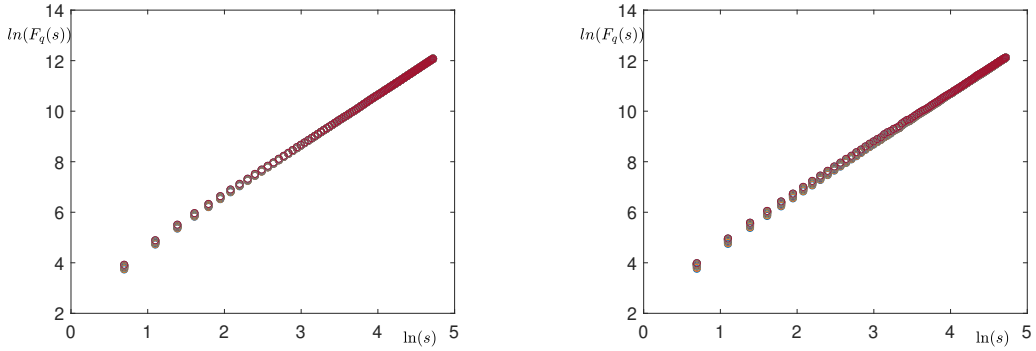

Figure 20: Double logarithmic function diagram of (a) normal hepatic cell, (b) hepatic cell of fatty liver.

As MF-DFA can express multifractality, scale in-variance and correlation of exchange rate time series, to emerge the degree of multifractal property, we calculate the Hurst index $h(q)$ versus q for each image, see Figure 21. From the Hurst exponential curve, we define the degree of multifractality by the following equation

$$\Delta h=h(q_{min})-h(q_{max}). \tag{5.1}$$

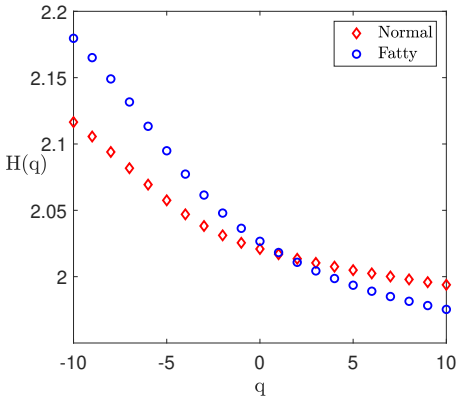

Figure 21: Hurst exponent of hepatic cells.

We calculate Δh for each image, Δh of normal hepatic cell image and the hepatic cell image of fatty liver are 0.0401 and 0.0619, respectively. We also list the data related to the multifractality

in Table 1. We find that with the increase of q, the range of $h(q)$ fluctuation of fatty liver image is larger, which indicates its multifractal characteristic is stronger and the multifractality of the normal hepatic cell image is more stable.

According to (2.12), we can acquire multifractal spectrum α and $f(\alpha)$. The multifractality spectra are marked by rhombus and circle symbol respectively. The width of the curve on the α axis represents the degree of the multifractal. A higher $\Delta\alpha$ indicates the time series has a stronger multifractal property. In Figure 22, it shows huge difference in the spans of the two multifractal singularity indicators between the two images. Δf and $\Delta\alpha$ in fatty liver image are greater than those in normal hepatic cell image, which explains that the multifractality of the normal hepatic cell image is more stable, this is consistent with what the Hurst index shows.

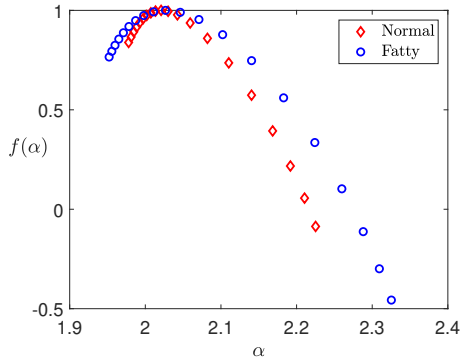

Figure 22: Multifractal spectrum of hepatic cells.

Both the $f(\alpha)$ spectra for the two images are shown as "left hook" shape, which explains that tendencies of the gray values are strengthened in both of the two images. Meanwhile, it also illustrates that singularity of the gray values in fatty liver image is more violent, which is consistent with the original image and the segmentation results are shown in Figure 19.

Table 1: Multifractality.

	Normal	Fatty
Hurst exponent $\Delta h(q)$	0.0401	0.0619
Multifractality degree $\Delta\alpha$	0.0847	0.1446

Subsequently, we apply our model to practical engineering applications. The detection of icing on transmission lines is of great importance in the power system. Firstly, icing can significantly increase the weight of transmission lines, which may cause the load on the towers to exceed their design range, leading to collapse or damage. Secondly, icing may alter the shape and position of power transmission lines, affecting their safe distance from adjacent lines or the ground, and increasing the risk of short circuits and fires. In addition, icing may also affect the conductivity of transmission lines, leading to a decrease in energy transmission efficiency and even causing power outages. Therefore, timely and accurate detection of icing on transmission lines is crucial for ensuring the safe and stable operation of the power system. Next, we verify the effectiveness of the

model for segmenting transmission lines under icing conditions. Figure 23(a) shows the original image, Figure 23(b) represents the segmentation mesh condition using the proposed algorithm, and Figure 23(c) exhibits the final segmentation image. The original image size is 225×225. In addition, the other parameters can be chosen as $v\times v=7\times7$, $q=-10$, and the segment scales s varies from 2 to 3.

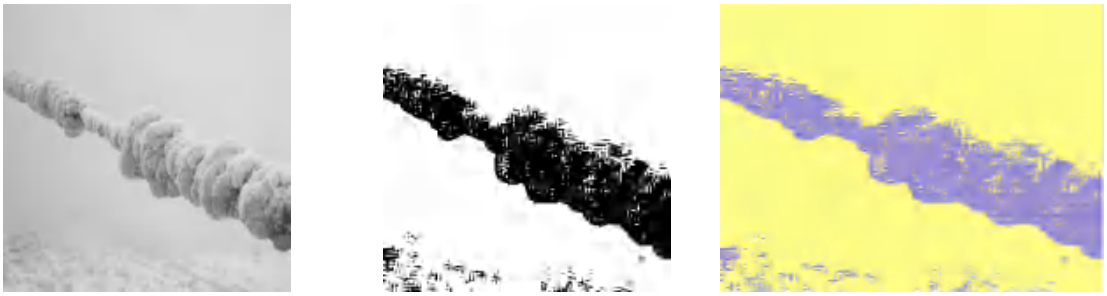

(a) (b) (c)

Figure 23: Transmission lines under icing conditions. (a) shows the original image, (b) represents the segmentation mesh condition using the proposed algorithm, and (c) exhibits the final segmentation image.

6 Conclusions

In this paper, we described 1D and 2D MF-DFA methods in detail. We briefly reviewed the applications of 1D MF-DFA, such as the fields in financial markets, energy markets, heartbeat, and atmospheric science. In addition, 2D MF-DFA has been studied for image segmentation,and medical image classification. We also provided empirical research of 1D and 2D MF-DFA methods. We choose the daily closing price of gold price in Korean market for 1D multifractal analysis. The results showed that there exists power law behavior and multifractal features of gold price. Besides, the gold price time series displayed persistent behaviors. Furthermore, the multifractal spectrum curve with left hook shape indicated that the probability of gold price at the highest price is greater than that at the lowest price, which means the price of gold at present is at a high level. Afterwards, we applied the 2D MF-DFA method for the study of images edge detection. We used the simple synthetic grid image, license plate, and hepatic cell images, and the segmentation results of these images showed the robustness and efficiency of 2D MF-DFA method. In addition, through the analysis of multifractality degree of hepatic cells, we found the multifractality of the normal hepatic cell image is more stable, which means the singularity of the gray values in fatty liver image is more pronounced. In the future, we may include more types of datasets to perfect our experiments and thus expand our analysis to global markets, exploring new fields such as ecological data and medical imaging, developing user-friendly tools, using diverse image datasets for validation, implementing real-time analysis, and encouraging interdisciplinary collaboration to innovate and expand multifractal analysis applications.

Acknowledgment

This paper is supported by the Management Technology Project of State Grid Liaoning Electric Power Co., LTD. Project number: 2023ZX-05.

Conflicts of Interest

The authors declare no conflict of interest.

References

[1] J. W. Kantelhardt, S. A. Zschiegner, and E. Koscielny-Bunde, Multifractal detrended fluctuation analysis of nonstationary time series, *Phys. A*, 2002, 316: 87–114.
[2] S. Lahmiri, Multifractal analysis of moroccan family business stock returns, *Phys. A*, 2017, 486: 183–191.
[3] G. Cao, Multifractal structure in china's foreign exchange market, In *2010 Int. Conf. E-Product E-Service E-Entertainment*, pages 1–4. IEEE, 2010.
[4] H. M. Niere, Measuring efficiency of international crude oil markets: A multifractality approach, *Int. J. Mod. Phys. Conf. Ser.*, 2015, 36: 1560013.
[5] S. Lahmiri and S. Bekiros, Chaos, randomness and multi-fractality in bitcoin market, *Chaos Soliton Fract.*, 2018, 106: 28–34.
[6] K. Matia, Y. Ashkenazy, and H. E. Stanley, Multifractal properties of price fluctuations of stocks and commodities, *Europhys. Lett.*, 2003, 61(3): 422,
[7] S. Drożdż, R. Kowalski, P. Oświecimka, R. Rak, and R. Gebarowski, Dynamical variety of shapes in financial multifractality, *Complexity*, 2018, 7015721.
[8] W. Shao and J. Wang, Does the "ice-breaking" of south and north korea affect the south korean financial market?, *Chaos Soliton Fract.*, 2020, 132: 109564.
[9] S. Lahmiri and S. Bekiros, Decomposing the persistence structure of islamic and green cryptocurrencies with nonlinear stepwise filtering, *Chaos Soliton Fract.*, 2019, 127: 334–341.
[10] H. T. Chen, R. B. Gu, and D. Q. Zhou, Multifractal analysis of international crude oil prices based on mf-dfa, *Complex Syst. Complex. Sci.*, 2009, 6(3): 40–49.
[11] X. Li, M. Zheng, J. Pu, Y. Zhou, W. Hong, X. Fu, and P. Ran, Identification of abnormally expressed lncrnas induced by $pm_{2.5}$ in human bronchial epithelial cells, *Biosci. Rep.*, 2018, 38(5): BSR20171577.
[12] J. Wang, J. Kim, and W. Shao, Investigation of the implications of "haze special law" on air quality in south korea, *Complexity*, 2020, 2020(1): 6193016.
[13] J. Wang, W. Shao, and J. Kim, Cross-correlations between bacterial foodborne diseases and meteorological factors based on mf-dcca: A case in south korea, *Fractals*, 2020, 28(03): 2050046.
[14] J. Wang, W. Shao, and J. Kim, Multifractal detrended cross-correlation analysis between respiratory diseases and haze in south korea, *Chaos Soliton Fract.*, 2020, 135: 109781.
[15] P. C. Ivanov, L. A. N. Amaral, A. L. Goldberger, S. Havlin, M. G. Rosenblum, Z. R. Struzik, and H. E. Stanley, Multifractality in human heartbeat dynamics, *Nature*, 1999, 399: 461–465.
[16] J. Gierałtowski, D. Hoyer, F. Tetschke, S. Nowack, U. Schneider, and J. Żebrowski, Development of multiscale complexity and multifractality of fetal heart rate variability, *Auton. Neurosci.*, 2013, 178: 29–36.

[17] K. Zhang, L. Ma, C. Cao, J. Yang, Z. Zhang, and Y. Chen, A skew normal mixture model with noise estimation for image segmentation, *J. Info. Comput. Sci.*, 2020, 17: 118–137.
[18] Q. Wang and J. Yang, Eye location and eye state detection in facial images with unconstrained background, *J. Info. Comput. Sci.*, 2016, 1(5): 284–289.
[19] I. Ismail, G. S. Eltaweel, and H. Nassar, Bands detection and lanes segmentation in dna fingerprint images, *J. Info. Comput. Sci.*, 2014, 9(4): 243–251.
[20] H. Chen and Z. Chen, Noise separation from multiple copy images using the fastica algorithm, *J. Info. Comput. Sci.*, 2011, 6(2): 143–151.
[21] P. Grassberger, An optimized box-assisted algorithm for fractal dimensions, *Phys. Lett. A*, 1990, 148: 63–68.
[22] C. Jin, H. Huang, and K. Liu, Medical image segmentation based on multifractal theory, *Chin. J. Tissue Eng. Res.*, 2010, 14: 1535–1538.
[23] L. Yu and D. Qi, Applying multifractal spectrum combined with fractal discrete brownian motion model to wood defects recognition, *Wood Sci. Technol.*, 2011, 45: 511–519.
[24] G. F. Gu and W. X. Zhou, Detrended fluctuation analysis for fractals and multifractals in higher dimensions, *Phys. Rev. E*, 2006, 74: 061104.
[25] G. F. Gu and W. X. Zhou, Detrending moving average algorithm for multifractals, *Phys. Rev. E*, 2010, 82: 011136.
[26] W. Shi, R. B. Zou, F. Wang, and L. Su, A new image segmentation method based on multifractal detrended moving average analysis, *Physica A Stat. Mech. Appl.*, 2015, 432: 197–205.
[27] F. Wang, Q. Fan, and H. E. Stanley, Multiscale multifractal detrended-fluctuation analysis of two-dimensional surfaces, *Phys. Rev. E*, 2016, 93: 042213.
[28] F. Wang, J. W. Li, W. Shi, and G. P. Liao, Leaf image segmentation method based on multifractal detrended fluctuation analysis, *J. Appl. Phys.*, 2013, 114: 214905.
[29] Y. E. Yu, F. Wang, and L. L. Liu, Magnetic resonance image segmentation using multifractal techniques, *Appl. Surf. Sci.*, 2015, 356: 266–272.
[30] J. Wang, W. Shao, and J. Kim, Combining mf-dfa and lssvm for retina images classification, *Bio. Sig. Process. Cont.*, 2020, 60: 101943.
[31] L. Zunino, B. M. Tabak, A. Figliola, D. G. Pérez, M. Garavaglia, and O. A. Rosso, A multifractal approach for stock market inefficiency, *Phys. A*, 2008, 387: 6558–6566.
[32] Q. Ruan, W. Jiang, and G. Ma, Cross-correlations between price and volume in chinese gold markets, *Phys. A*, 2016, 451: 10–22.
[33] C. Maillo, J. Martín, D. Sebastian, M. Hernandez-Alvarez, M. Garcia-Rocha, O. Reina, and R. Mendez, Circadian-and upr-dependent control of cpeb4 mediates a translational response to counteract hepatic steatosis under er stress, *Nat. Cell Biol.*, 2017, 19: 94.